Sensors and Materials, Vol. 38, No. 6 (2026) 3301–3314
MYU Tokyo

S & M 4504

Optical Nondestructive Metrology of High-aspect-ratio Micro-holes via Focus-displacement Mapping

Birui Wu,* Wenle Lan, Ying Chen, Lifeng Wang, and Guoxiang Liang

School of Mechanical and Electrical Engineering, Ningde Normal University, Ningde, Fujian 352100, China

(Received January 19, 2026; accepted May 28, 2026)

Keywords: aspect ratio, nondestructive measurement, OV7725 CMOS, STM32H743, shape from focus

The accurate and efficient metrology of micro-holes with aspect ratios from 5:1 to 20:1 remains challenging owing to low throughput and a high risk of damage in conventional approaches. Here, we develop an embedded optical, nondestructive measurement system that exploits a focus-displacement mapping mechanism to quantify key geometric parameters of high-aspect-ratio micro-holes. We introduce a gradient-variance-driven adaptive sharpness operator (GDANS) and a three-point parabolic interpolation scheme to rapidly locate focal planes with subpixel precision. In addition, a lightweight random sample consensus（RANSAC)-based circle fitting routine is employed to extract diameter and circularity with high efficiency. The system is built around an STM32H743 microcontroller and integrates an OV7725 CMOS image sensor, a quasi-coaxial illumination path, and a high-precision geared motor module through a modular opto-mechatronic design. A state-machine-based software architecture enables closed-loop operation from autofocus scanning to parameter reporting. Experiments on calibrated samples demonstrate favorable performance in measurement speed, cost, and practical deployability, providing a feasible solution for the rapid on-site inspection of high-aspect-ratio micro-holes in industrial settings.

1. Introduction

Micro-hole structures are fundamental building blocks in three-dimensional integrated circuits (3D ICs), MEMS, and precision medical devices, where they enable electrical interconnects, fluid transport, and mechanical support. The geometric fidelity of these micro-holes directly affects device performance and long-term reliability.[1–3] In particular, blind micro-holes with aspect ratios exceeding 10:1 have become central to advanced packaging and 3D integration because of their superior vertical interconnection capability and efficient use of space.[4,5] Nevertheless, the fast, nondestructive, and accurate measurement of micro-hole morphological characteristics—such as depth, diameter, and circularity—remains a critical bottleneck for manufacturing quality control and industrial deployment.[6,7] Existing metrology approaches include contact probing, SEM, and laser confocal microscopy.[8] Contact probing can deliver high absolute accuracy but suffers from low throughput and can mechanically damage

*Corresponding author: e-mail: 89630871@qq.com
https://doi.org/10.18494/SAM6178

ISSN 0914-4935

fragile sidewalls, rendering it unsuitable for in-line inspection.[9–12] SEM provides nanometer-scale surface resolution; however, it typically requires vacuum operation and often involves destructive sample preparation, preventing *in situ* nondestructive measurement. Although laser confocal microscopy is noncontact, it becomes unreliable for blind holes with aspect ratios above ~10:1 because multiple reflections and strong attenuation inside deep cavities markedly reduce the signal-to-noise ratio (SNR) at the bottom, compromising measurement fidelity.[13,14] The proposed X-ray micro-computed tomography-based method enables the detection of machining accuracy in printed circuit board (PCB) array holes, yet it is limited by insufficient resolution, difficulty in distinguishing composite materials, and the need for small sample sizes to achieve high precision.[3] To address these challenges, we build an embedded optical metrology system based on the classical principle of shape from focus (SfF).[15–18] The key contribution is not a new optical principle, but rather, a system-level solution tailored to high-aspect-ratio blind-hole imaging under stringent constraints of embedded real-time processing and low cost.[19] Specifically, we tackle degraded bottom imaging quality and the limited robustness of conventional SfF operators by proposing gradient-variance-driven adaptive sharpness operator (GDANS) with adaptive evaluation windows. Together with efficient three-point parabolic refinement and lightweight random sample consensus (RANSAC) circle fitting, the approach delivers practical accuracy while meeting real-time requirements. On the implementation side, the system integrates an STM32H743 microcontroller, an OV7725 CMOS sensor, and a compact quasi-coaxial optical path into a low-cost prototype suitable for industrial environments. Software is organized as a state-machine-driven modular pipeline that automates scanning, processing, and reporting.

Compared with the aforementioned techniques, our system is explicitly positioned along the following axes: (i) cost and simplicity—the total component cost is approximately USD 50–80, which is two orders of magnitude lower than that of high-end commercial instruments (typically USD 50000–80000); (ii) throughput—the automated measurement completes in below 10 s, with manual alignment adding approximately 12 s, supporting rapid on-site inspection; (iii) applicable range—the method is validated for aspect ratios from 5:1 to 20:1, with depths up to 5 mm and diameters down to ~0.1 mm.

2. System Architecture

Figure 1 illustrates the developed optical nondestructive measurement system for high-aspect-ratio micro-holes. The system adopts a compact modular design with an overall size of 136.06 × 100.00 × 100.00 mm^3 and consists of four major subsystems: an optical imaging module, a motion-control module, an image-processing module, and an embedded control unit.

2.1 Optical imaging module

The optical module comprises an OV7725 high-sensitivity CMOS image sensor, an imaging barrel, a beam splitter, and an LED illumination source. Collimated light from the LED is reflected downward by a 45° plate beam splitter to illuminate the micro-hole surface. The

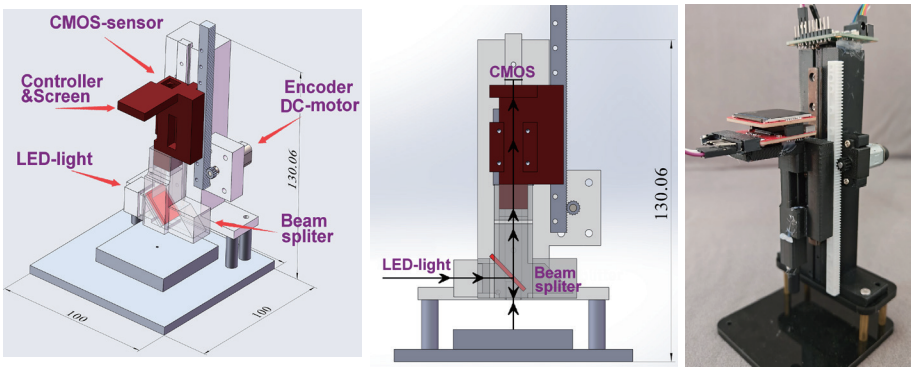

Fig. 1. (Color online) 3D CAD model and prototype of the proposed micro-hole metrology system.

reflected light passes back through the beam splitter and is imaged by the CMOS sensor, forming a quasi-coaxial epi-illumination configuration. This architecture effectively suppresses stray light, improves edge contrast, and is particularly advantageous for inspecting blind micro-holes with large aspect ratios.

2.2 Motion-control module

The motion module employs a miniature narrow linear guide, a rack-and-pinion mechanism, and a geared motor to drive the imaging unit along the vertical axis. The combination of the linear guide and rack transmission provides high rigidity, low friction, and good perpendicularity, enabling the stable acquisition of focus stacks during axial scanning.

2.3 Mechanical integration

The structure was parametrically modeled and assembled in SolidWorks. Components were fabricated using fused deposition modeling (FDM) with polyethylene terephthalate glycol (PETG), which provides adequate mechanical strength, thermal resistance, and dimensional stability for the rapid prototyping of precision motion parts. This integrated opto-mechatronic design coordinates illumination, image acquisition, and precision displacement control, providing a robust hardware foundation for SfF-based 3D reconstruction.

3. Core Algorithmic Framework

The system quantifies 3D morphology using a focus-displacement mapping strategy. During scanning, the imaging unit is translated along the optical axis so that the micro-hole top and bottom surfaces are sequentially brought into focus. The corresponding axial coordinates are recorded, and their difference yields the micro-hole depth. From the best-focus images, the system further extracts edge contours at the entrance and bottom planes to compute diameter and circularity.[18,20] The algorithm comprises two lightweight modules optimized for the embedded real-time execution of (i) focus evaluation and depth localization, and (ii) rapid geometric parameter extraction.

3.1 Focus evaluation and depth localization

During axial scanning, the images acquired at successive positions are assessed using a focus metric, and the best-focus planes for the top and bottom surfaces are identified. High-aspect-ratio blind holes present heterogeneous image characteristics: the entrance region typically exhibits rich texture and high contrast, whereas the bottom suffers from illumination attenuation, low contrast, and poor SNR. Fixed-window focus measures can therefore be unreliable. To improve robustness, we propose GDANS, an adaptive-window operator driven by local gradient variance.

For a grayscale image $I(x, y)$, we compute approximate horizontal and vertical gradients using a simplified Sobel operator:

$$\begin{cases} G_x(x,y) = I(x+1,y) - I(x-1,y), \\ G_y(x,y) = I(x,y+1) - I(x,y-1). \end{cases} \tag{1}$$

For a local window centered at pixel (x, y) with size $(2\omega + 1) \times (2\omega + 1)$, the local focus measure is defined as

$$F(x,y) = \sum_{i=-w}^{w} \sum_{j=-w}^{w} \left[G_x^2(x+i,y+j) + G_y^2(x+i,y+j) \right]. \tag{2}$$

To adapt to different texture regimes, GDANS dynamically adjusts the window size $W = 2\omega + 1$ on the basis of the gradient variance σ_{G2} within the window:

$$W = \begin{cases} 5, & \sigma_G^2 < T_1 \\ 9, & T_1 \le \sigma_G^2 < T_2 \\ 13. & \sigma_G^2 \ge T_2 \end{cases} \tag{3}$$

Here, T_1 and T_2 are the thresholds determined via calibration (typical values are $T_1 = 5$ and $T_2 = 15$, corresponding to smooth and edge-rich regions, respectively).

During scanning at axial positions z_k, the system computes the average focus score $\overline{F}(Z_k)$ over a region of interest (ROI), forming a focus curve that exhibits a pronounced unimodal peak near the true focal plane. To refine the peak location efficiently, we use three-point parabolic interpolation. Let the peak sample and its neighbors be $\left(z_1, \overline{F}_1\right)$, $\left(z_2, \overline{F}_2\right)$, and $\left(z_3, \overline{F}_3\right)$ with $\overline{F}_2 > \overline{F}_1$ and $\overline{F}_2 > \overline{F}_3$. The refined best-focus position z_{focus} is

$$z_{focus} = z_2 + \frac{(\overline{F}_1 - \overline{F}_3)(z_2 - z_1)}{2(\overline{F}_1 - 2\overline{F}_2 + \overline{F}_3)}. \tag{4}$$

This refinement uses only basic arithmetic and is therefore well suited to the STM32H743 floating-point unit.[21] The micro-hole depth is computed from the difference between the best-focus positions of the top and bottom surfaces:

$$H = z_{focus}^{(bottom)} - z_{focus}^{(top)}, \tag{5}$$

where $z_{focus}^{(top)}$ and $z_{focus}^{(bottom)}$ are obtained from the motor encoder or step pulse counts converted to physical displacement.

3.2 Rapid geometric parameter extraction

Given the best-focus images for the entrance and bottom planes, the system extracts contours and computes diameter and circularity. Edge extraction is performed using a lightweight Canny detector with adaptive threshold selection to obtain closed contours at the entrance and bottom. The contour pixels are resampled at uniform angular increments to generate an ordered point set $P = \{p_i = (x_i, y_i) \mid i = 1, 2, \ldots, N\}$.

A simplified RANSAC circle fitting procedure robustly estimates the circle center (x_c, y_c) and radius R. In each iteration, three non-collinear points are randomly sampled from P to compute candidate circle parameters by solving

$$\begin{cases} (x_1 - x_c)^2 + (y_1 - y_c)^2 = R^2, \\ (x_2 - x_c)^2 + (y_2 - y_c)^2 = R^2, \\ (x_3 - x_c)^2 + (y_3 - y_c)^2 = R^2. \end{cases} \tag{6}$$

To reduce computation, an algebraic elimination yields a direct closed-form solution without matrix inversion. For each candidate, radial residuals $d_i < \delta$ are computed for all points, and the number of inliers satisfying $d_i = \left| \sqrt{(x_i - x_0)^2 + (y_i - y_0)^2} - R \right|$ is counted. After M trials ($M = 12$ in this system), the candidate with the maximum inlier count is selected.

The circularity error ε quantifies the deviation of the measured contour from an ideal circle. A computationally efficient approximation is adopted.

$$\varepsilon = \max_i \sqrt{(x_i - x_c)^2 + (y_i - y_c)^2} - \min_i \sqrt{(x_i - x_c)^2 + (y_i - y_c)^2} \tag{7}$$

This avoids iterative optimization, substantially reducing computational load while maintaining engineering accuracy for real-time embedded reporting.

4. Hardware Design

The hardware is modular and centered on image acquisition (OV7725), motion control, and data processing. The system consists of a main control unit (STM32H743), an image sensor module, a motor drive module, and power management. The block diagram is shown in Fig. 2.

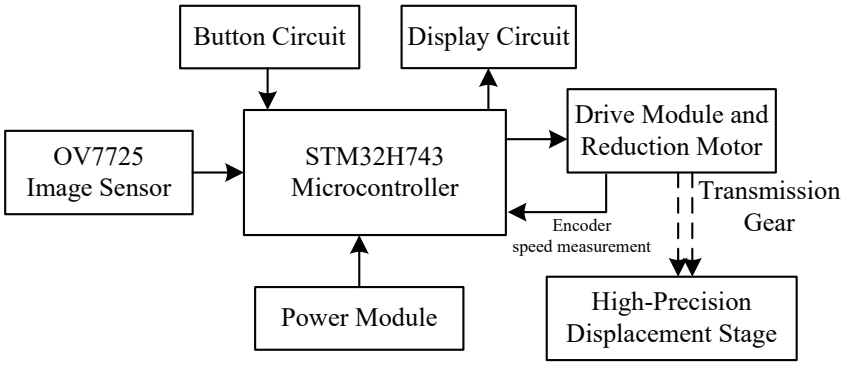

Fig. 2. System block diagram.

4.1 Main control unit

We select the STM32H743 high-performance microcontroller (LQFP100). With an Arm Cortex-M7 core running up to 480 MHz, the chip integrates a double-precision hardware floating-point unit and DSP instructions, enabling the efficient execution of focus evaluation, depth fitting, and geometric computation.[21] Its digital camera interface (DCMI) supports direct high-speed acquisition from OV7725 with low latency. The abundant peripherals allow flexible expansion: two SPI interfaces drive two LCDs, where a 240 × 240 display visualizes the micro-hole image and focus status in real time, and an 80 × 160 display is dedicated to numerical results for effective human–machine interaction. High-resolution timers generate precise PWM signals for the displacement motor, enabling accurate scan synchronization. On-chip memory stores calibration coefficients and measurement records. Figure 3 shows the minimal system schematic.

4.2 Image sensing and processing

The OV7725 CMOS image sensor provides up to 640 × 480 resolution with a pixel size of 6.0 × 6.0 μm. The sensor integrates programmable gain amplification (PGA), automatic exposure control (AEC), and automatic white balance (AWB), improving robustness under variable illumination. It interfaces with STM32H743 via DCMI for reliable low-latency streaming. With the optimized quasi-coaxial epi-illumination path (optical axis alignment error < 0.05° and working distance of 35 mm), the system maintains a stable illumination of no less than 300 lux at the bottom of micro-holes as deep as 20 mm, enabling usable bottom imaging. Figure 4 shows the imaging circuit schematic.

5. Software Design

The software runs on STM32H743 and adopts a modular state-machine architecture to implement a closed-loop pipeline from autofocus scanning to parameter output. The main flow

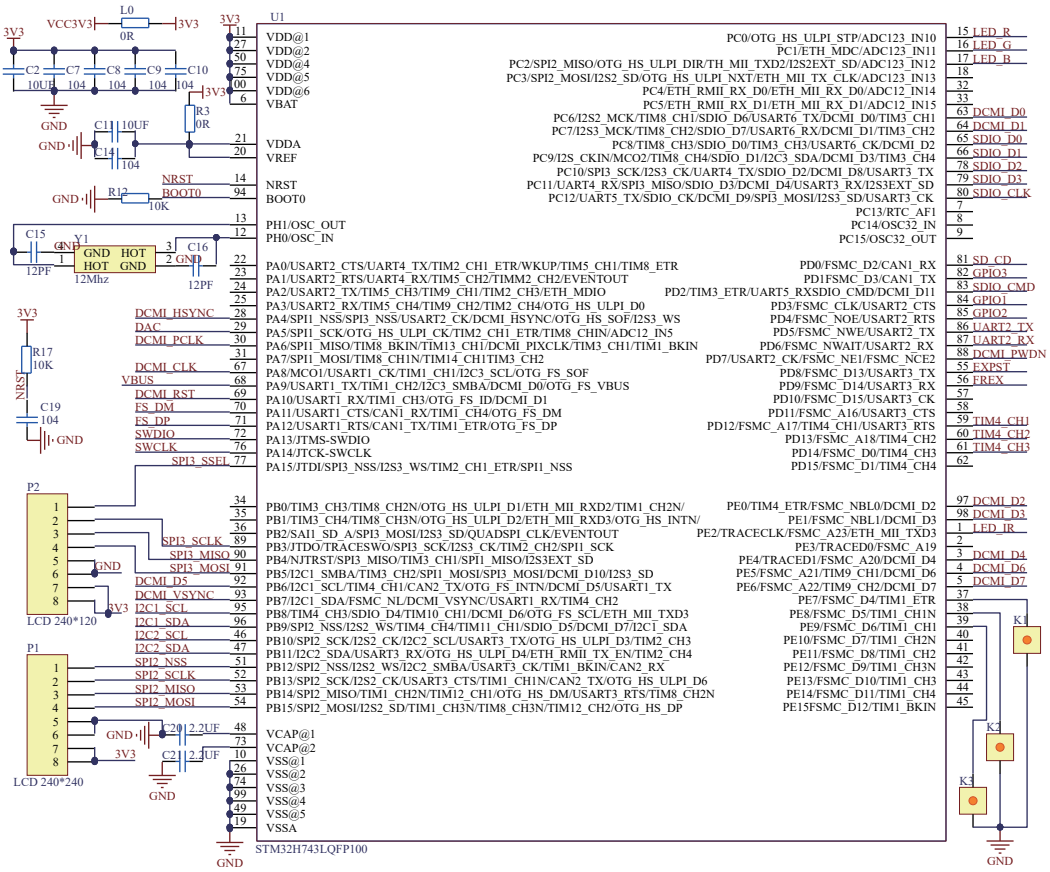

Fig. 3. (Color online) Minimal system schematic of the STM32H743.

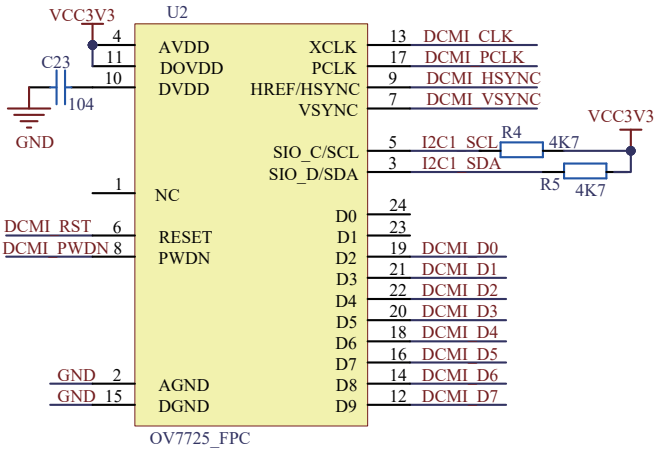

Fig. 4. (Color online) Schematic of the image acquisition circuit.

(Fig. 5) consists of system initialization, scan control, image processing, and parameter estimation. After turning on the power, the system configures OV7725, loads LV8548MC motor

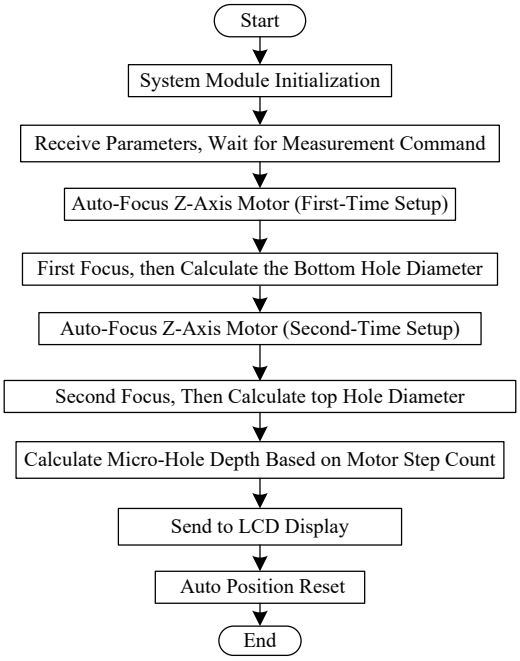

Fig. 5. Software flow chart of the main program.

parameters, initializes dual LCDs, and loads calibration coefficients. It then enters an idle state awaiting a trigger from the touchscreen.

Upon receiving a measurement command, the system enters the scan mode. The imaging unit first returns to a home position to establish a reference plane. It then steps along the optical axis toward the sample while acquiring frames via DCMI. For each frame, the GDANS focus score is computed over the ROI. The system monitors the focus trend in real time: the first detected local maximum is assigned to the bottom focal plane and the corresponding motor pulse count N_{bottom} is recorded. The bottom contour is extracted from that frame and fit by the simplified RANSAC to yield the bottom diameter D_{bottom}. The scan continues until a second focus maximum is detected and assigned to the top focal plane; the pulse count N_{top} is recorded and the top diameter D_{top} is estimated similarly. The scan then terminates.

During parameter estimation, micro-hole depth is computed from the pulse difference using a calibrated pulse-to-displacement conversion coefficient k_p (calibrated as $5/(380 \times 44)$ mm per pulse in the source text).

$$H_n = k_p \cdot | N_{bottom} - N_{top} | \tag{8}$$

The hole diameter is taken as the arithmetic mean of $D_n = \frac{D_{top} + D_{bottom}}{2}$. The aspect ratio for each sample was calculated using the formula $aspect\ ratio = \frac{H_n}{D_n}$. This approach was adopted because the micro-holes exhibit a slight taper due to the laser drilling process, and the average diameter provides a representative characteristic dimension for calculating the effective aspect ratio. For

the measured values, the aspect ratio and its standard deviation were propagated from the depth and diameter measurements using standard error propagation formulas.

To achieve the target throughput (a full single-hole measurement within ~10 s), multiple optimizations are implemented: the focus metric uses 16-bit fixed-point multiply–accumulate operations; image transfer is handled via DMA to reduce CPU overhead; and circle fitting and depth estimation leverage the hardware FPU. Results—depth, diameter, aspect ratio, and circularity—are refreshed in real time on the LCD and can be streamed to a host PC via serial communication. The system then automatically resets and waits for the next measurement, completing a fully automated "acquire-process-display" loop.

6. Experiments and Analysis

To validate the measurement accuracy of the proposed system, a series of standard micro-hole samples was fabricated by direct laser ablation on 304 stainless steel substrates using a laser system operating at a wavelength of 1.06 μm. This fabrication approach was selected to produce micro-holes with well-defined edges and consistent geometric features, thereby establishing a reliable basis for subsequent comparative measurements. Ground-truth values of the micro-hole geometries were calibrated using a commercial high-precision area-confocal three-dimensional microscope (3D Sensing Technology Co., Ltd., China). Reference measurements of depth and diameter were obtained with an accuracy higher than 1 μm, ensuring a robust benchmark for system validation.

The alignment procedure is as follows. First, the camera height is adjusted to bring the sample surface into sharp focus. The sample stage is then manually positioned using a mechanical fixture to center the micro-hole within the camera's field of view (FOV), guided by real-time visual feedback from the imaging system. Once the hole is approximately centered, the software automatically defines an ROI around the hole to isolate it from the background for subsequent analysis. The system then executes the measurement algorithm to compute the depth, diameter, and circularity of the micro-hole.

To evaluate the overall performance, five sets of standard micro-hole samples with known geometry were measured repeatedly. Under identical environmental conditions, each sample was measured five times by the proposed system, and the average was reported. The measurement results for the physical prototype are shown in Fig. 6 (as referenced in the source

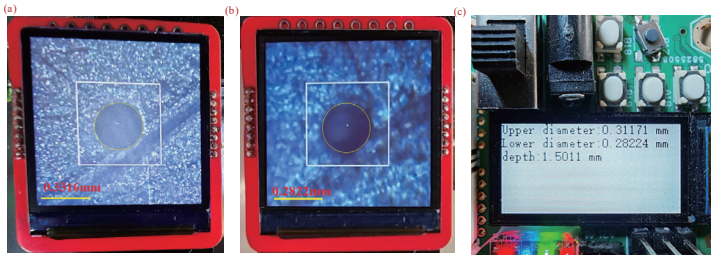

Fig. 6. (Color online) Experimental results of micro-hole measurement. (a) Top surface measurement image. (b) Bottom surface measurement image. (c) Visualized calculated parameters.

text; figure numbering is retained as provided), and key parameters are summarized in Table 1. Figure 7 presents the relative focus measure as a function of depth (*Z*-axis position).

To assess practical throughput, the time required for each operational step was measured under typical conditions. An experienced operator consistently completed manual *X*–*Y* alignment within 12 s. The subsequent automated measurement—including ROI definition and algorithm execution—was accomplished below 10 s, yielding a total cycle time of approximately 22 s per sample. In addition, the effect of *X*–*Y* misalignment on measurement accuracy was systematically examined through controlled experiments with varying degrees of off-center positioning. Misalignment within ±50 μm was found to have negligible effects on diameter and circularity measurements, with relative errors remaining below 2%. By contrast, larger misalignments risk compromising ROI definition and degrading focus detection, particularly for high-aspect-ratio micro-holes. These findings highlight the importance of precise alignment and support the retention of the manual alignment step in the current workflow.

Table 1
Measured depth, top and bottom diameters, and aspect ratio of high-aspect-ratio micro-holes obtained by the proposed SFF-based method (*mean* ± *SD*, $n = 5$).

Sample	Value type	Depth (mm)	Top diameter (mm)	Bottom diameter (mm)	Aspect ratio (%)
1	Ground truth	1.5246	0.3146	0.3026	4.9403
	Measured	1.5363	0.3187	0.2995	4.9702
2	Ground truth	1.6785	0.2546	0.2355	6.8496
	Measured	1.6566	0.2516	0.2398	6.7424
3	Ground truth	1.9778	0.1549	0.1355	13.621
	Measured	1.9461	0.1581	0.1321	13.412
4	Ground truth	2.5785	0.2495	0.2186	11.017
	Measured	2.5196	0.2466	0.2239	10.710
5	Ground truth	3.1454	0.2147	0.1896	15.559
	Measured	3.2358	0.2109	0.1954	15.928
6	Ground truth	3.9723	0.23145	0.17565	19.515
	Measured	4.1057	0.23848	0.18134	19.454

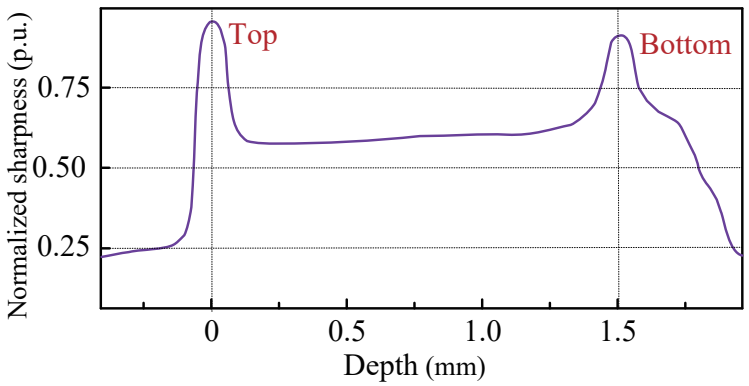

Fig. 7. (Color online) Normalized focus measure as a function of depth.

Figure 8 presents the bar chart of relative measurement errors. Overall, the system exhibits good consistency and repeatability across all samples. The relative error of depth remains within ±3.2%. For diameter, the error of the top diameter is within ±2.0%, and the bottom diameter error does not exceed ±3.3%. The computed aspect ratios follow the trend of the reference values, with a maximum deviation below 4.8%. While the absolute accuracy does not yet match high-end professional metrology instruments, the proposed system provides compelling advantages in throughput, system cost, integration density, and on-site usability.

To evaluate the repeatability of the proposed measurement system, five independent measurements (n = 5) were conducted on each sample under identical conditions. For each measured parameter—including depth, top diameter, bottom diameter, and aspect ratio—the mean, standard deviation (*SD*), coefficient of variation (*CV*%), and 95% confidence interval (*CI*) were calculated. These statistical results have been incorporated in this manuscript, with detailed data for Sample 1 presented in Table 2.

As summarized in the newly added statistical analysis, all *CV*% values for Sample 1 are below 3%, indicating excellent measurement repeatability. Furthermore, even for Sample 6—which exhibits a higher aspect ratio—*CV*% remains below 4.8%. This demonstrates that the proposed method maintains stable and reliable performance under more demanding measurement conditions.

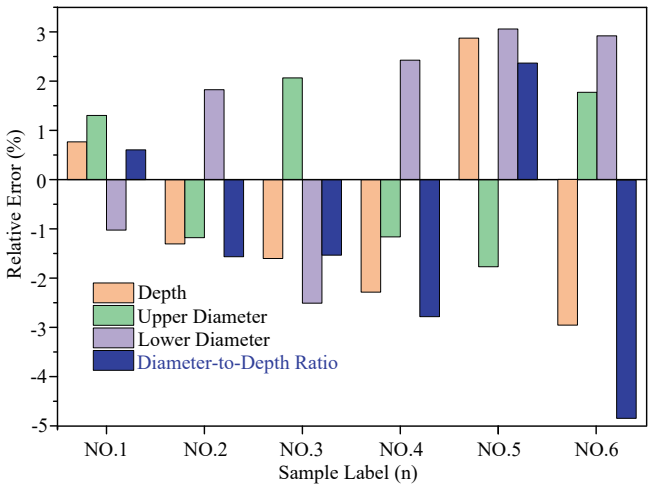

Fig. 8. (Color online) Bar chart of relative measurement errors.

Table 2
Statistical analysis of repeated measurements (n = 5) for Sample 1.

Parameter	*Mean*	*SD*	*CV* (%)	95% Confidence interval
Depth (mm)	1.5246	0.0174	1.14	[1.5030, 1.5462]
Top diameter (mm)	0.3187	0.0089	2.80	[0.3076, 0.3298]
Bottom diameter (mm)	0.2995	0.0077	2.58	[0.2899, 0.3091]
Aspect ratio	4.933	0.077	1.56	[4.8374, 5.0286]

The system uses an N20 encoder DC geared motor with a 380:1 reduction ratio. In the described configuration, 44 PWM pulses correspond to one rotor revolution; after the gearbox, one output-shaft revolution produces 5 mm of axial travel. Therefore, the theoretical axial displacement per PWM pulse is $5/(380 \times 44) \approx 2.99 \times 10^{-4}$ mm, which yields a theoretical depth resolution of approximately 3×10^{-4} mm. Measurement errors arise from multiple sources, including optical diffraction limits, mechanical positioning error, algorithmic approximation, and environmental disturbances. The diffraction-limited resolution is estimated as

$$\delta_{diff} \approx \frac{0.61\lambda}{NA}. \tag{9}$$

For λ = 550 nm and the numerical aperture of 0.15, the source text reports $\delta_{diff} \approx 2.24$ μm. Mechanical positioning errors are mitigated by a bidirectional approach strategy and can be limited to ±0.8 μm. Algorithmic errors introduced by Gaussian-blur approximations and three-point parabolic interpolation are estimated at approximately ±1.2 μm. Temperature fluctuations can be compensated by

$$\Delta L = \alpha \cdot L_0 \cdot (T - T_{ref}), \tag{10}$$

where α is the thermal expansion coefficient and T_{ref} = 20 °C is the calibration temperature. A linear correction model between measured and true values is obtained via calibration experiments:

$$M_{true} = k \cdot M_{meas} + b. \tag{11}$$

Using the data provided in Table 1 as an example, the calibration coefficients for depth measurement were preliminarily obtained through linear regression, yielding approximately $k \approx 0.997$ and $b \approx -0.0023$ mm. In practical engineering applications, a more comprehensive multipoint calibration was performed using additional reference samples to ensure the validity of these coefficients across the entire measurement range. The coefficients k and b are stored in STM32H743 Flash for real-time correction, improving absolute accuracy under hardware constraints. The system completes the full-parameter measurement of a single hole within ~10 s and is well suited to rapid nondestructive screening and process monitoring in production environments.

The total component cost of our system is approximately USD 50–80, which is two orders of magnitude lower than the USD 50000–80000 price range of high-end commercial instruments. However, we acknowledge that this cost reduction comes with certain performance trade-offs. Specifically, our system employs off-the-shelf lenses with a lower imaging resolution than specialized optics and utilizes a standard rack-and-pinion mechanism driven by a DC motor for vertical scanning, which inherently exhibits a greater absolute positioning error than precision-ground screw drives. Additionally, while high-end instruments integrate automated *XY* stages

with pattern recognition algorithms to precisely center the micro-hole within the FOV, our system requires manual *XY* adjustment by the operator—a process that introduces additional setup time and operator dependency.

The method is applicable to micro-holes with depths up to ~5 mm, diameters of approximately 150–320 μm, and aspect ratios ranging from 5:1 to 20:1. Beyond this range—particularly for aspect ratios exceeding 20:1—the SNR at the bottom surface becomes insufficient for reliable focus detection. Optimal performance is achieved on opaque or semi-reflective surfaces with moderate roughness. Highly specular surfaces may introduce glare, while excessively rough or absorptive materials, such as carbon composites, can degrade edge contrast and compromise focus measure reliability. In deep holes with aspect ratios greater than 15:1, signal attenuation reduces gradient variance, resulting in a flatter focus curve and an increased likelihood of peak misdetection. Although the proposed GDANS operator mitigates this effect, it does not fully eliminate errors under extreme SNR degradation. A misalignment within ±50 μm has a negligible impact on measurement accuracy (relative error < 2%). However, larger misalignments (>100 μm) may lead to partial ROI truncation, incorrect edge detection, and shifts in focus peak position, particularly for small-diameter holes. The ROI must fully enclose the micro-hole; otherwise, background noise may contaminate the focus evaluation. Peak misdetection can also occur when the focus curve exhibits multimodality caused by spurious reflections or debris inside the hole.

7. Conclusions

We developed an embedded optical, nondestructive metrology system for micro-holes with aspect ratios from 5:1 to 20:1, on the basis of a focus-displacement mapping principle. Using quasi-coaxial epi-illumination and a modular opto-mechatronic design, the system integrates an OV7725 CMOS sensor and a geared motor module, and performs real-time processing on an STM32H743 platform from image acquisition and focus evaluation to geometric parameter estimation. Algorithmically, we proposed GDANS with adaptive windows, combined with three-point parabolic refinement for subpixel focus localization, enabling the robust identification of best-focus planes for both the entrance and bottom surfaces. Micro-hole depth is obtained directly from the motor displacement, and diameters and circularity are computed efficiently via lightweight RANSAC circle fitting. Although there remains a gap in absolute accuracy compared with high-end instruments, the proposed solution offers clear advantages in speed, cost, integration, and nondestructive operation, making it suitable for rapid on-site inspection and in-line process monitoring.

Acknowledgments

This work was supported by The Talent Introduction Program of Ningde Normal University (grant number 2024Y05). The authors would like to thank the editors and reviewers for their valuable comments and suggestions.

References

1 L. Zheng, Y. Li, Z. Sun, Y. Luo, Y. Xu, J. Wang, C. Wang, and X. Wei: Chin. J. Mech. Eng. **38** (2025) 1. https://doi.org/10.1186/s10033-025-01245-3
2 T. Hovell, J. Petzing, W. Guo, C. Gill, L. Justham, N. Lohse, and P. Kinnell: Metrology. **3** (2023) 139. https://doi.org/10.3390/metrology3020009
3 W. Tao, Y. Xu, H. Liu, C. Wang, and L. Zheng: Micron. **131** (2020) 102826. https://doi.org/10.1016/j.micron.2020.102826
4 B. Xia, L. Jiang, X. Li, X. Yan, W. Zhao, and Y. Lu: Applied Physics A. **119** (2014) 61. https://doi.org/10.1007/s00339-014-8955-5
5 J. Cui, L. Li, J. Li, and J. B. Tan: Sens. Actuators **190** (2013) 13. https://doi.org/10.1016/j.sna.2012.10.030
6 S. Barman, N. Hanumaiah, and A. B. Puri: Int. J. Adv. Manuf. Technol. **76** (2013) 115. https://doi.org/10.1007/s00170-013-5243-z
7 E. Peiner and L. Doering: Microsyst. Technol. **16** (2009) 1259. https://doi.org/10.1007/s00542-009-0951-x
8 T. Sajima, H. Murakami, A. Katsuki, and D. Tabuchi: Sens. Mater. **24** (2012) 10. https://doi.org/10.18494/sam.2012.777
9 H. Liu, J. Bai, B. Zhang, Y. Cao, S. Hou, and Z. Zhou: Int. J. Adv. Manuf. Technol. **119** (2021) 615. https://doi.org/10.1007/s00170-021-08205-w
10 L. Doering, U. Brand, S. Bütefisch, T. Ahbe, T. Weimann, E. Peiner, and T. Frank: Meas. Sci. Technol. **28** (2017) 1. https://doi.org/10.1088/1361-6501/28/3/034009
11 S. Elfurjani, J. Ko, and M. B. G. Jun: Meas. Sci. Technol. **89** (2016) 215. https://doi.org/10.1016/j.measurement.2016.04.023
12 Y. Nagasu, K. Eguchi, K. Itoh, M. Otani, and N. Nakayama: J. JSEM. **14** (2014) 5. https://doi.org/10.11395/jjsem.14.s105
13 X. Chen, Y. Xu, N.-K. Chen, S. Shy, and H.-C. Chui: Photonics **8** (2021) 1. https://doi.org/10.3390/photonics8110493
14 J. Ranjan, K. Patra, T. Szalay, M. Mia, M. K. Gupta, Q. Song, G. Krolczyk, R. Chudy, V. A. Pashnyov, and D. Y. Pimenov: Sensors (Basel). **20** (2020) 1. https://doi.org/10.3390/s20030885
15 Z. Fan, M. Xia, B. Dong, G. Yan, W. Guo, K. Yang, and W. Li: Meas. Sci. Technol. **34** (2023) 1. https://doi.org/10.1088/1361-6501/acdf0e
16 E. Edrei and G. Scarcelli: ACS Photonics. **7** (2020) 914. https://doi.org/10.1021/acsphotonics.0c00109
17 D. Luo, T. Längle, and J. Beyerer: tm - Technisches Messen. **84** (2017) 452. https://doi.org/10.1515/teme-2017-0007
18 S. Pertuz, D. Puig, and M. A. Garcia: Pattern Recognit. **46** (2013) 1415. https://doi.org/10.1016/j.patcog.2012.11.011
19 B. Winiarski and P. J. Withers: Exp. Mech. **52** (2011) 417. https://doi.org/10.1007/s11340-011-9502-3
20 C. C. Kao and A. J. Shih: Meas. Sci. Technol. **18** (2007) 3603. https://doi.org/10.1088/0957-0233/18/11/045
21 STMicroelectronics. STM32H743xx Reference Manual (2023). STM32Cube - Discover the STM32Cube Ecosystem - STMicroelectronics